De-solvation of metal complexes to construct metal-organic framework glasses

Yong-Sheng Wei[1]*, Zeyu Fan[2], Cheng Luo[2], Satoshi Horike[1,2,3]*

[1]Institute for Integrated Cell-Material Sciences, Institute for Advanced Study, Kyoto University, Yoshida-Honmachi, Sakyo-ku, Kyoto 606-8501, Japan

[2]Department of Synthetic Chemistry and Biological Chemistry, Graduate School of Engineering, Kyoto University, Katsura, Nishikyo-ku, Kyoto 615-8510, Japan

[3]Department of Materials Science and Engineering, School of Molecular Science and Engineering, Vidyasirimedhi Institute of Science and Technology, Rayong, 21210, Thailand

*Email: horike@icems.kyoto-u.ac.jp (S.H.); wei.yongsheng.3t@kyoto-u.ac.jp (Y.-S.W.)

Abstract: Structural fine-tuning is an important challenge in the glass sciences including metal-organic framework (MOF) glasses. Current approaches of thermally/mechanically-induced vitrification are limited for azolate/cyanide-based crystalline MOFs, while other MOF crystals usually decompose before melting or upon milling instead of forming stable glasses. Here, we developed a general method, "de-solvation" of solvated metal-ligand discrete complexes to gently prepare MOF glasses by demonstrating 12 ligands of varying lengths, shapes, side- and coordination-groups (carboxylate/pyridyl/azolate). Hydrogen-bond networks of the metal complexes offer the spatial arrangements of metal-ligand units, thus guiding the glass formations during de-solvation. The prepared glasses have structural diversities with tunable pores (sizes and modifications) and dimensionalities (one to three), and high glass-forming abilities with wide glass transition temperatures from 120 to 280 ˚C, affording grain-boundary-free/transparent monoliths under heating without pressure.

INTRODUCTION

Glass is non-crystalline inorganic, organic or metallic solids, offering versatile fundamental sciences and applications in industry. Recently, an emerging class of metal-organic framework (MOF) glasses provides unlimited possibilities for systematically altering chemical composition, topology, and functionality of glasses (*1, 2*). An important consideration in tuning such structural diversity and property is to carry out design principles from crystalline MOFs (*3*). One ideal strategy for this is to construct carboxylate MOF glasses because carboxylate ligands, featuring rich building blocks and functional modifications (Fig. S1) (*4*), have been widely employed for MOF crystal engineering (*5*). However, challenges arise when targeting carboxylate MOF glasses. Current preparations rely mainly on thermally/mechanically-induced vitrification of MOF crystals (*6-14*), while carboxylate MOFs will decompose before melting or upon milling instead of forming stable glasses (*15-17*).

Herein we demonstrate a general synthesis, that is, a de-solvation strategy for metal complexes working as precursors to create carboxylate MOF glasses (Figs. S2 and S3). The discrete metal complexes are generally stacked together to form crystals in an energetically favorable way, where coordinated/lattice solvents stabilize the assembled structures by introducing multiple intermolecular forces (*18*). In other words, de-solvation will break the interactions and thereby structural rearrangements of metal ions with ligands occur toward metastable states (*19*). Based on this, bridging carboxylate ligands designedly employed in given metal complexes will prefer to connect with the metal ions of adjacent metal complexes to form metastable metal-ligand networks, thus offering a promising path for various carboxylate MOFs to enter their glass states.

RESULTS AND DISCUSSION

Synthesis and structure of metal complexes

We study the de-solvation strategy with a series of metal complexes using 12 different organic linkers with a range of size, modification, and complexity (Figs. 1A, S4 and Table S1). The four ligands are linear pyridinecarboxylic acids: isonicotinic acid (HL1), 3-(pyridin-4-yl)acrylic acid (HL2), 4-(pyridin-4-yl)benzoic acid (HL3), and (*E*)-4-(2-(pyridin-4-yl)vinyl)benzoic acid (HL4) with increasing lengths offer evolutive structural flexibilities. Modifications of halogens (F, Cl and Br) and amino group (-NH_2) on HL1 give 3-fluoroisonicotinic acid (HL5), 3-chloroisonicotinic acid (HL6), 3-bromoisonicotinic acid (HL7) and 3-aminoisonicotinic acid (HL8), providing a configurational control between carboxylate and pyridine ring. In addition to the linear pyridine-carboxylate linkers, this approach led us to access bent ligands with different coordinating groups: nicotinic acid (HL9), 4-(1*H*-imidazol-1-yl)benzoic acid (HL10), 2-(3-(pyridin-4-yl)-1*H*-

1,2,4-triazol-5-yl)pyridine (HL11) and 3-methyl-2-(3-(pyridin-4-yl)-1H-1,2,4-triazol-5-yl)pyridine (HL12), to realize the dimensional control in glass construction.

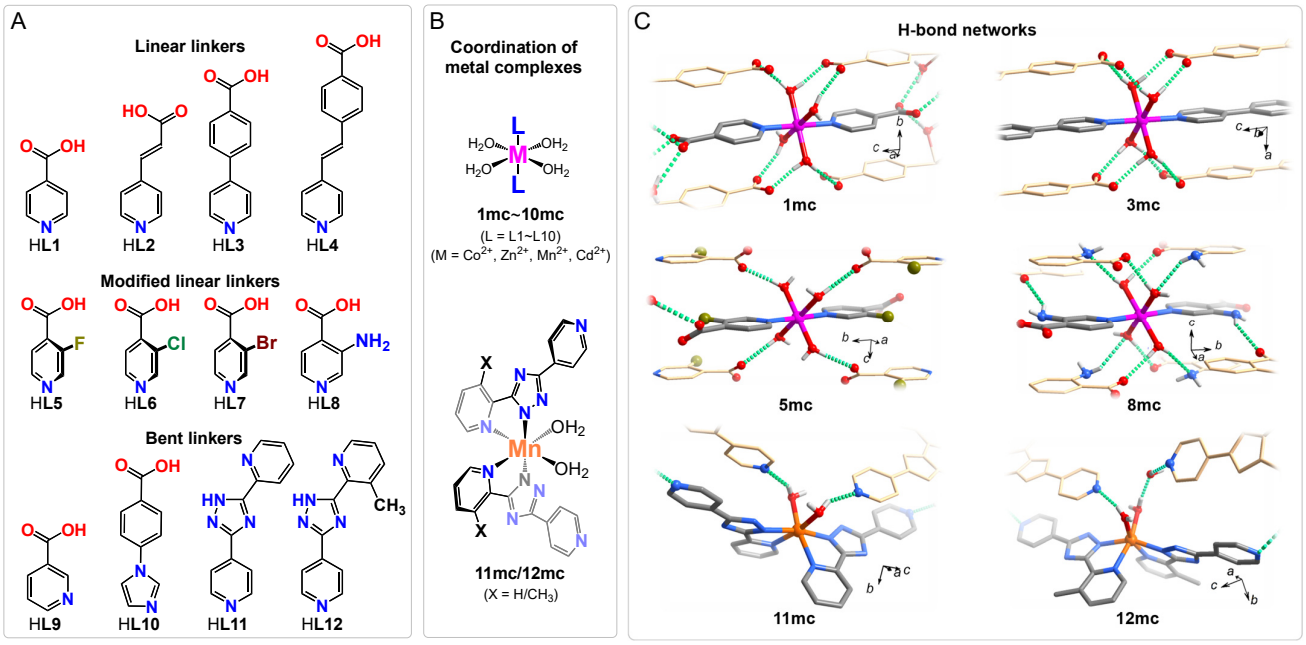

Fig. 1. Structures of ligands and metal complexes as precursors for MOF glasses. The structures of (**A**) ligands and (**B**) representative metal complexes. (**C**) Partial structures of the hydrogen-bond networks based on the metal complexes. Color code: Co purple, Mn brown, C grey, N blue, O red, F chartreuse, H white. Green dotted lines represent strong hydrogen bonds in the networks.

Room-temperature (RT) reactions of HL1~HL12 ligands with metal ions in alkaline aqueous solutions yielded 12 crystalline products of the metal complexes (Figs. 1B and 1C). Single-crystal X-ray diffraction (SCXRD) analyses confirmed that hydrogen-bond networks based on mononuclear metal complexes are the structural features (Table S2), where coordinated H_2O molecules and uncoordinated groups of ligands serve as bridging donor and acceptors, respectively (Fig. 1C). Hereafter, ***x*mc**, ***x*g**, ***x*sl**, and ***x*c** are employed to denote the **metal complexes**, **glassy**, **supercooled liquid** and **crystallized MOFs**, respectively, where the *x* is the number of samples. In the cases of **1mc~10mc** with a common formula $[Co(L)_2(H_2O)_4]$, Co(II) is octahedrally occupied by two nitrogen atoms of two pyridine (py) groups in apical positions and four water molecules in equatorial plane (Figs. 1B and S5). The carboxyl groups are deprotonated as counter anions while uncoordinated to the Co(II) ions. The four coordinated water molecules are hydrogen-bonded (O–H···O) by at least four different carboxyl oxygens from adjacent metal complexes (Fig. S5B). π–π stacking interactions of the conjugate rings of ligands allow these discrete units to be connected into a layered structure (Fig. S5C). The adjacent layers are linked through hydrogen-bonded interactions (O···H–C) between coordinated waters (acceptors) and conjugate rings (donors), forming three-dimensional (3D) networks (Fig. S5D). Both of Mn(II) centers in $[Mn(L11)_2(H_2O)_2]\cdot 3H_2O$·(**11mc**) and $[Mn(L12)_2(H_2O)_2]\cdot 3H_2O$·(**12mc**) are coordinated by two H_2O

molecules and four nitrogen atoms from two L11/L12 in distorted octahedral N_4O_2 geometries (Fig. 1B). The two complexes feature uncoordinated pyridyl groups, hydrogen-bonded (N···H–O) by the coordinated water molecules from the neighboring metal complexes, resulting in 1D structures along the *c*-axis (Fig. 1C).

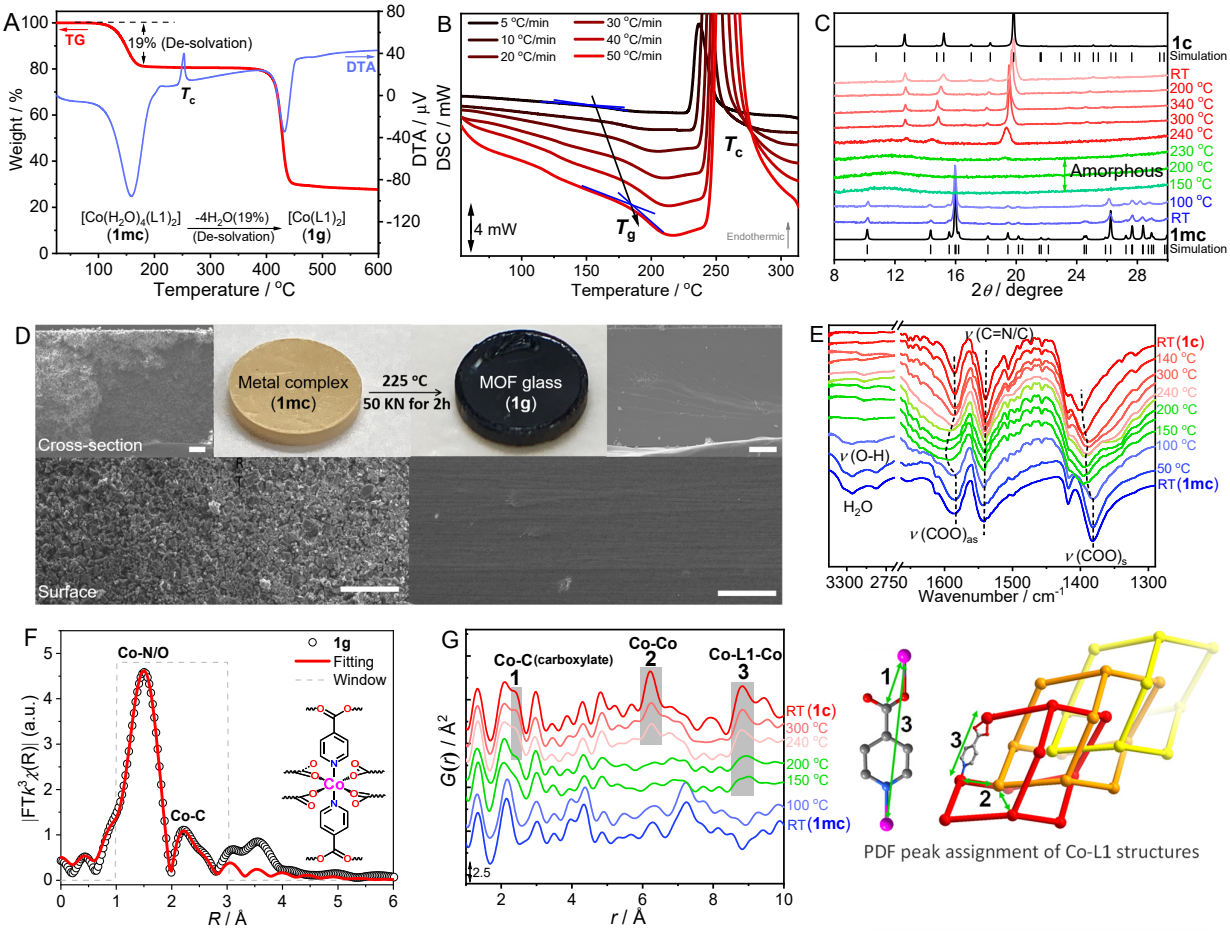

Fig. 2. De-solvation of 1mc to form 1g. (**A**) TG-DTA profiles. (**B**) DSC profiles at different heating rates of 5~50 °C·min^{-1} to distinguish T_g. (**C**) Variable temperature PXRD patterns. (**D**) Optical images of **1mc** pellet (Φ: 5 mm) and hot-pressed **1g** monolith (225 °C and 50 KN for 2 hours) and the corresponding SEM images of the surface and cross-section. Scale bar = 50 μm. (**E**) Variable temperature FT-IR spectra upon **1mc**. The peak shifts are highlighted by the dotted lines. (**F**) Co *K*-edge EXAFS fitting curve of **1g**. Insert: proposed architecture of the coordination environment around Co(II). (**G**) Variable temperature PDF profiles upon **1mc** with the peak assignment of structures.

De-solvation of 1mc to form 1g

De-solvation of the metal complexes was performed by heating samples under inert atmosphere. **1mc** was employed as the representative case to describe the glass-forming behavior (Fig. 2). Thermogravimetry (TG) curve showed the coordinated water molecules were completely removed before 170 °C (Fig. 2A), yielding an amorphous phase of [Co(L1)$_2$] (**1g**). Differential scanning calorimetry (DSC) for **1g** revealed an explicit endothermic peak related to glass transition and a based-line shifting at the glass transition temperature (T_g) of 173 to 185 °C was observed when varying the heating rate from 5 to 50 °C min^{-1} (Figs. 2B and S6). DSC determined an intense crystallization peak (T_c) at 243 °C during further heating. Variable temperature powder

X-ray diffraction (VT-PXRD) confirmed the crystalline (**1mc**)-amorphous (**1g**)-crystalline (**1c**) transformations (Fig. 2C). Another important characteristic of glass is the ability to fabricate a grain-boundary-free monolith. Pellet of **1mc** microcrystals was prepared and then vitrified by de-solvation at 200 °C for 30 min. The further hot-pressing technique yielded a monolith of **1g** under 50 kN and vacuum for 2 hours at 225 °C where is 52 ºC higher than T_g (Fig. 2D). Scanning electron microscopy (SEM) images confirmed that the glassy monolith had a crack-free and smooth surface, while the precursor pellet showed nanoparticles separated by grain-boundaries.

The glass nature of **1g** prompted us to investigate its intrinsic coordination and topology structures. Structural comparison between **1mc** and **1c** will be essential to understand the glass structure. **1mc** has been solved by SCXRD and **1c** was identified as a reported diamondoid (**dia**)-topological structure in 3-fold interpenetration (Fig. S7) (*20*). **1c** has a 4-connected [Co(py)$_2$(carboxylate)$_2$] node in an octahedral geometry, where the two pyridine and two chelating carboxylates come from four different L1$^-$ linkers. Considering the persistent connection of Co-py during heating, the investigation of metal-carboxylate coordination modes is of importance in understanding the glass structure.

Energy difference in Fourier transform-infrared spectroscopy (FT-IR) between ν(COO)$_s$ and ν(COO)$_{as}$ (s/as = symmetry/asymmetry) vibrations has been widely used to reveal the coordination mode of carboxylates (*21*). As shown in variable temperature FT-IR (VT-FTIR) at RT (Fig. 2E), a broad band at 3500–2750 cm^{-1} are indicative of the coordinated water molecules. The difference ($\Delta\nu$ = 200 cm^{-1}) between ν_{as}(COO) = 1583 and ν_s(COO) = 1383 cm^{-1} in **1mc** is consistent with the presence of ionic carboxylates (Fig. S8). When heating to 150 °C, all coordinated water molecules were removed and $\Delta\nu$ increased up to 210 cm^{-1}, indicating that carboxylates changed to bridging coordination in **1g** (*22*). Meanwhile, the broadening peak of ν_{as}(COO) at 1600 cm^{-1} is observed to support the structural disorder, suggesting the glass nature of **1g**. Further heating to 240 °C led to the crystallization with narrowing peaks of ν_{as}(COO) at 1584 cm^{-1} and smaller $\Delta\nu$ = 185 cm^{-1}, which consists with the chelating mode in the **1c**. It should be noted that the peak of ν(C=N/C) at 1540 cm^{-1} were almost unchanged during heating, demonstrating the thermal robustness of metal-pyridine coordination.

Coordination structure details were further investigated by X-ray absorption fine structure (XAFS) analysis. The identical profiles of X-ray absorption near-edge structure (XANES) with a distinguishable pre-edge peak at 7707 eV (1*s*→3*d* transitions) suggested that Co ions in three phases retains the oxidation state of +2 (Fig. S9A). However, the extended X-ray absorption fine structure (EXAFS) of **1g** is distinctly different with these of **1mc** and **1c** (Fig. S9B). The FT (Fourier transformed)-EXAFS of **1g** in *R* space from 1.0 to 3.0 Å was well fitted by use of the proposed Co(py)$_2$(carboxylate)$_4$ moiety (Figs. 2F and S9C), giving fitted Co-O distances of 2.07±0.07 and Co-N distance of 1.94±0.10 Å (Table S3). Considering all the Co(II) in glass are

coordinated by two pyridine rings and four bridging carboxylates from six different $L1^-$ linkers, **1g** should be a 3,6-connected coordination polymer of $[Co(L1)_2]$.

Pair distribution functions (PDF) analyses derived from synchrotron X-ray total scattering from RT to 300 ˚C upon **1mc** were taken to provide more detailed structural evolution. As shown in Fig. 2G, **1mc** remained stable until 100 ˚C, consisting with the TG and FT-IR results. With heating up to 150 ˚C (de-solvation), the *G*(r) become nearly featureless at r >10 Å, demonstrating the absence of long-range order in the **1g** (Fig. S10). Besides, peaks at 2.4 and 8.8 Å started to appear, which correlate with Co-carboxylate (Co-C) and Co-L1-Co connection, respectively, indicating the network formation in glassy phase. Under further heating above 240 ˚C toward crystallization, a new peak appeared at 6.2 Å corresponding the distance between two Co(II) from adjacent **dia** networks (calc. 6.2 Å), suggesting the different topologies of **1g** from **1c**.

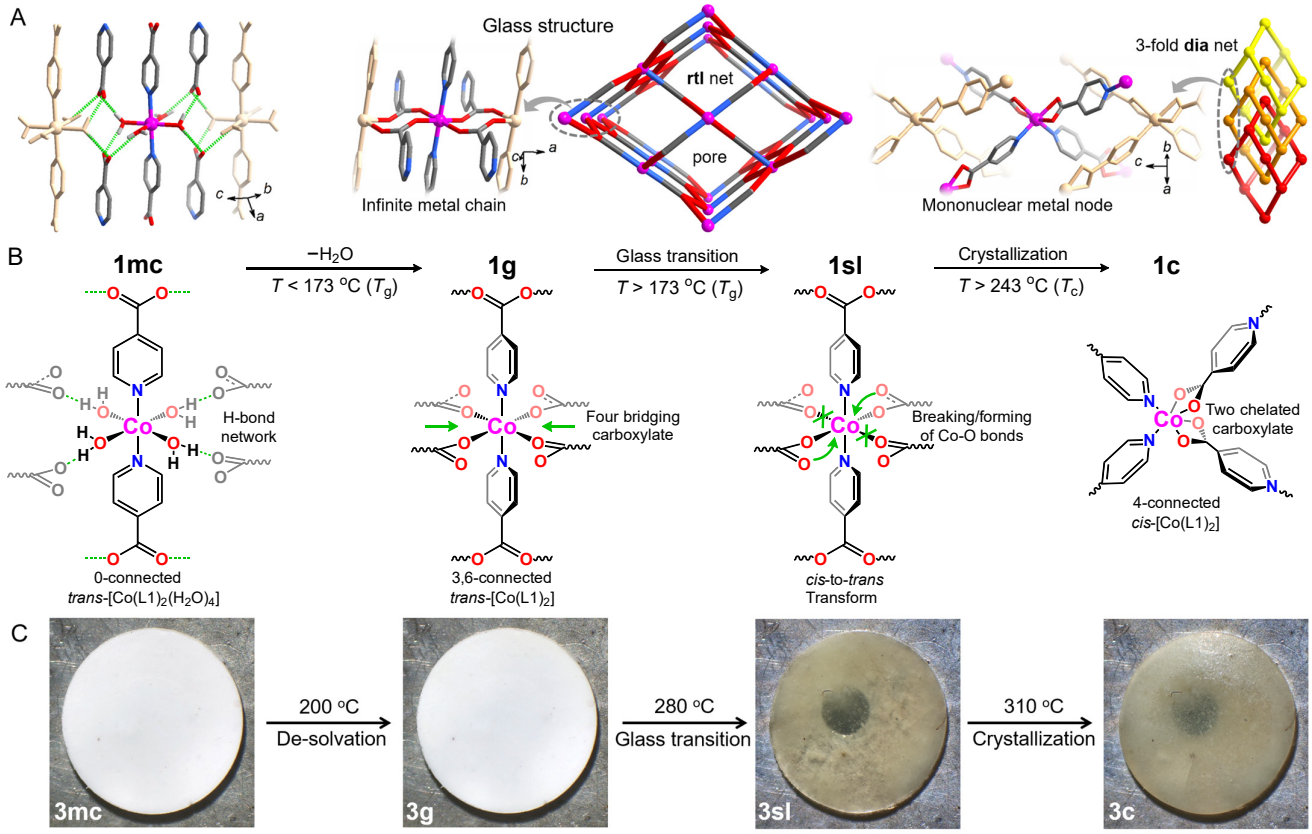

Fig. 3. Structural transformation during de-solvation and crystallization. (**A**) Crystal structures of the **1mc** (left) and **1c** (right) as well as the proposed structure of **1g** (middle) from crystalline $[Co(L1)_2]$. Color code: Co purple, C grey, N blue, O red, H white. (**B**) Proposed transformation of coordination environments around Co(II) upon de-solvation and crystallization processes. (**C**) Optical images of heat-induced transformation from pellet of **3mc** (Cd analogue), pellet of **3g** upon de-solvation, transparent monolith of **3sl** upon glass transition, finally to semi-transparent monolith of **3c** upon crystallization. The diameter of the starting pellet (**3mc**) is 5.0 mm and the black spot behind the monolith were introduced to evaluate the transparency.

Based on the above evidences, the thermal transformation from discrete complex to polymeric glass may

undergo the following way (Fig. 3). Guided by the hydrogen bonds, the coordinated H_2O removal of *trans*-[Co(L1)$_2$(H_2O)$_4$] (**1mc**) allows oxygen atoms of carboxylate groups to directly connect with the released Co(II) site from adjacent metal complexes. Based on the spatial arrangements of Co(II) and $L1^-$ in **1mc** (Fig. 3A), we speculate that carboxylates in *trans*-[Co(L1)$_2$] (**1g**) bridge two neighboring metal ions to form a 1D indefinite chain of [Co(py)$_2$(carboxylate)$_2$] (Fig. 3B). The adjacent chains are connected to each other by $L1^-$ ligands, forming a 3,6-connected rutile (**rtl**)-topological 3D framework with 1D open pores in the glass state, suggested by a reported analogous of crystalline [Co(L1)$_2$] with same PXRD patterns (Figs. S11 to S13) (*22, 23*). Structural comparison confirmed that the de-solvation changed partial pyridine-carboxylate configurations from a coplanar mode in **1mc** to a twisted one due to the coordination with Co(II) (Fig. S13). Further heating enabled **1g** to be destructed and transform into supercooled liquid state (**1sl**) that is a highly fragmented Co-L1 network, where the bridging coordination on one side between the distorted carboxylate and Co(II) was expectedly broken (*24*). **1sl** tended to maximize the packing efficiency (densification) through thermally structural rearrangements of Co(II) and $L1^-$, via *trans*-to-*cis* coordination transition, finally crystallized into the 3-fold nonporous **dia** topological structure of *cis*-[Co(L1)$_2$] (**1c**). These proposed structural transformations are supported by gas adsorption measurements (Fig. S14). **1mc** and **1c** that are nonporous showed negligible uptake of CO_2 at 195 K, while the porous **1g** exhibited a total uptake of 40.4 $cm^3\ g^{-1}$ at 1 bar with an apparent BET surface area of 130.5 $m^2\ g^{-1}$ and pore volume of 0.072 $cm^3\ g^{-1}$. This is slightly lower than 0.096 $cm^3\ g^{-1}$ calculated from the structure of crystalline [Co(L1)$_2$].

Table 1. Key parameters of the synthesized MOF glasses. T_g and T_c are the temperatures of glass transition and crystallization, respectively. Dashes indicate no reported MOF structures.

MOF glass	Net of glass	T_g / ˚C	T_c / ˚C	Net after crystallization	*Refs.* for the crystallized states
1g	**rtl** (3D)	173 148 (Zn) 231 (Mn) 225 (Cd)	243 225 (Zn) 256 (Mn) 264 (Cd)	3-fold **dia** (3D)	(*20*)
2g		225	256	5-fold **dia** (3D)	(*25*)
3g		280	314	6-fold **dia** (3D)	(*26*)
4g		257	337	8-fold **dia** (3D)	(*27*)
5g		120	208	**rtl** (3D)	(*28*)
6g		160	227		-
7g		170	252		-
8g		238	289	3-fold **dia** (3D)	-
9g	**ant** (3D)	140	214	**sql** (2D)	(*29*)
10g	**sql** (2D)	256	294		(*30*)
11g	1D chain	261	385		(*31*)
12g		225	300	2-fold **nbo** (3D)	(*32*)

Applicability of the de-solvation approach

De-solvation strategy is applicable to different metal ions, while the resultant MOF glass analogues upon the same ligand show different temperature windows (T_g to T_c) for supercooled liquids, such as **1g** series: 148 ~ 225 °C (Zn) < 174 ~ 243 °C (Co) < 231 ~ 256 °C (Mn) < 225 ~ 264 °C (Cd) (Table 1 and Fig. S15). The upward shifts follow the trend in ionic radii (pm) of $r_{Zn(II)}$ (74) < $r_{Co(II)}$ (74.5) < $r_{Mn(II)}$ (83) < $r_{Cd(II)}$ (95), and bond length (Å) of metal-pyridine (M-N): Zn-N: 2.1351(11) < Co-N: 2.1470(15) < Mn-N: 2.2703(10) < Cd-N: 2.3132(11) in the corresponding metal-L1 complexes. Larger ionic radius Cd(II) analogues has superior glass-formation ability that, under heating above T_g = 225 °C without any physical pressure, enables its precursor pellet to transform into a semitransparent one, which became a non-transparent pellet again upon further heating above T_c = 264 °C (Figs. S16 and S17). This phenomenon implies that higher crystallization temperatures of given glasses may favor the formation of grain-boundary-free monoliths.

Modifications of organic linkers also offer the opportunity to alter the glass property. Based on the HL1, three longer linear ligands of HL2, HL3, and HL4 were designed by addition of serial coplanar conjugated groups. We synthesized the three Co(II) complexes of **2mc**~**4mc** (Figs. 1C and S18 to S20) and then prepared the corresponding MOF glasses of **2g**~**4g** by de-solvation (Figs. S21 and S22). Compared with **1g**, these glasses should also feature the **rtl**-network due to the identical [Co(py)$_2$(carboxylate)$_2$] chain nodes confirmed by XAFS analysis (Fig. S23). DSC results demonstrated a general upward shift of temperature windows of T_g to T_c from 174 ~ 243 °C (**1g**), 225 ~ 256 °C (**2g**), 280 ~ 314 °C (**3g**) to 257 ~ 337 °C (**4g**) that follows the trend of their increasing ligand lengths from 4.9, 7.4, 9.2 to 11.5 Å (Fig. 1A). As a result, taking an example of **3g** with high T_c = 314 > 264 °C, its grain-boundary-free monolith was directly formed under heating over T_g without physical pressure (Figs. 3C and S16). The enhanced glass-formation ability implies that longer linkers have higher flexibility and stronger intermolecular interactions (e.g., π···π) among ligands lead to higher steric hindrances/barriers for structural rearrangement toward crystallization (*13, 33, 34*). Compared with the 3-fold **dia** nets of **1c**, the three above glasses also crystallized into **dia** topological networks while with enhanced degrees of interpenetrations (5, 6, 8-fold for **2c**, **3c**, **4c**, respectively) (Figs. S24 to S26) (*25-27*).

In addition to the efforts upon linear expansion, side group modifications (-F, -Cl, -Br and -NH$_2$) based on HL1 produce a configurational control of ligands to promisingly alter glass properties. For instance, the halogenated ligands of L5$^-$ ~ L7$^-$ within **5mc**~**7mc** showed energetically favored torsions (32.3°, 23.1° and 62.6°, respectively) between the uncoordinated carboxylate and pyridine ring compared with that (11.6°) of L1$^-$ (Figs. 1A and S27). The resulting low symmetry and high distortion probably weaken the intermolecular interactions among the ligands within glass states, thus giving the lower T_g of **5g** (120 °C), **6g** (160 °C) and **7g** (170 °C) than 174 °C of **1g** (Fig. S28). Unlike **1g** with reversibly twisted carboxylate group, VT-PXRD and

VT-FTIR demonstrated that the intrinsic distortion of these halogenated ligands allows the **rtl** network of glasses to be retained even after crystallization at T_c = 208, 227 and 252 ˚C, respectively (Figs. S29 to S31). The upward shifts of both T_g and T_c from **5g**, **6g** to **7g** follow the trend of F, Cl, and Br, indicating the higher reorganization energy of the ligands with heavier halogens (*35*). On the other hand, HL8 that has -NH_2 exhibits a coplanar conformation due to strong intramolecular hydrogen bond (N–H···O: 2.698(2) Å) with carboxylate (Figs. 1C and S27). Different from **5g**~**7g**, the obtained **8g** crystallized into the 3-fold **dia** topological network, but with higher T_g = 238 and T_c = 289 ˚C than these of **1g**, probably due to the decreased structural mobility caused by the strong intermolecular H-bond interactions (*36*). The higher T_c supports **8g** should have better glass-formation ability than that of **5g**~**7g** and **1g** (Fig. S32).

To further confirm generalizability of the de-solvation approach, we accessed other kinds of ligands with different shapes and coordination groups tune the structural dimensionalities of MOF glasses. Inspired by the linear ligands used above, a series of bent ligands (HL9~HL12) were employed to construct **9mc**~**12mc** (Figs. 1C and S33 to S36). TG-DTA, DSC and VT-PXRD confirmed their de-solvation and glass-formation behaviors (figs. S37 and S38). In the case of $L9^-$, by simply adjusting carboxylate group from para- to meta-position on the pyridine ring of $L1^-$, the resulting **9g** with T_g = 150 ˚C showed a different nonporous 3D network of **ant** topology based on a similar 1D chain node of [Co(py)$_2$(carboxylate)$_2$] compared with **1g** (Figs. S39 and S41) (*37, 38*). For the $L10^-$, by changing the pyridyl by imidazolate allows **10g** with T_g = 256 ˚C to feature 2D **sql** structure based on a discrete node of [Co(imidazolate)$_2$(carboxylate)$_2$] suggested by its crystallized state of **10c** owing to their identical XAFS and FT-IR spectra (Figs. S42 to S44). VT-PXRD confirmed that both **9g** and **10g** crystallized into 2D **sql** networks upon further heating over 214 and 294 ˚C, respectively (Figs. S4, S38, S40 and S42) (*29, 31*), indicating that the bent ligands dominate the thermally structural transitions during crystallization.

Apart from the carboxylate MOF glasses, de-solvation strategy is also applicable for nitrogen-donor ligand of HL11 to form **11mc**. After de-solvation, a transparent monolith was also formed under heating over T_g = 261 ˚C without physical pressure (Fig. 4). XAFS analysis demonstrated that the glass has a uniform 3-connected discrete node in rectangular pyramid Mn-N_5 geometry (Fig. 4A), although $L11^-$ potentially has multiple coordination modes with metal ions (Fig. S45). Besides, during heating upon **11mc**, the FT-IR peak of ν(C=N) correlating with pyridyl and triazolate groups exhibited a redshift from 1601, 1595 to 1592 cm^{-1} in two steps at 150 and 325 ˚C, which agrees well with **11mc**-to-**11g**&**11sl**-to-**11c** transformations (Fig. 4B). The other FT-IR peaks merely assigned to pyridyl groups gradually disappeared at 1569, 1504, 1458, 1415 cm^{-1} before 280 ˚C and new peaks appeared nearby at 1560, 1498, 1452, 1409 cm^{-1} after 150 ˚C, respectively. The presence of intersecting temperature ranges demonstrates that ligands of **11g**/**11sl** should possess both

uncoordinated and coordinated pyridyl groups. Based on the above analysis and H-bond network of **11mc**: *cis*-[Mn(L11)$_2$(H$_2$O)$_2$], the 3-connected discrete node should be linked by L10$^-$ with the coordinated pyridyl groups to probably form 1D chain coordination structures in the glass state (Fig. 4C) (*31*). Under further heating through **11sl** via *cis*-to-*trans* coordination transition, the adjacent chains were connected to each other by the uncoordinated pyridyl groups with the 3-connected Mn-N$_5$ unit to 4-connected Mn-N$_6$ node, finally forming a **sql**-topological framework of *trans*-[Mn(L11)$_2$] (**11c**) above 385 ˚C (Fig. S46). Compared with **11g**, **12g** should have a similar 1D coordination structure but a lower T_g = 225 ˚C due to the methyl modification (Figs. S47 to S49). Moreover, the **12g** crystallized into a 2-fold 3D **nbo** topological network at 300 ˚C because the methyl group changes the coordination direction of L12$^-$ (Figs. S50).

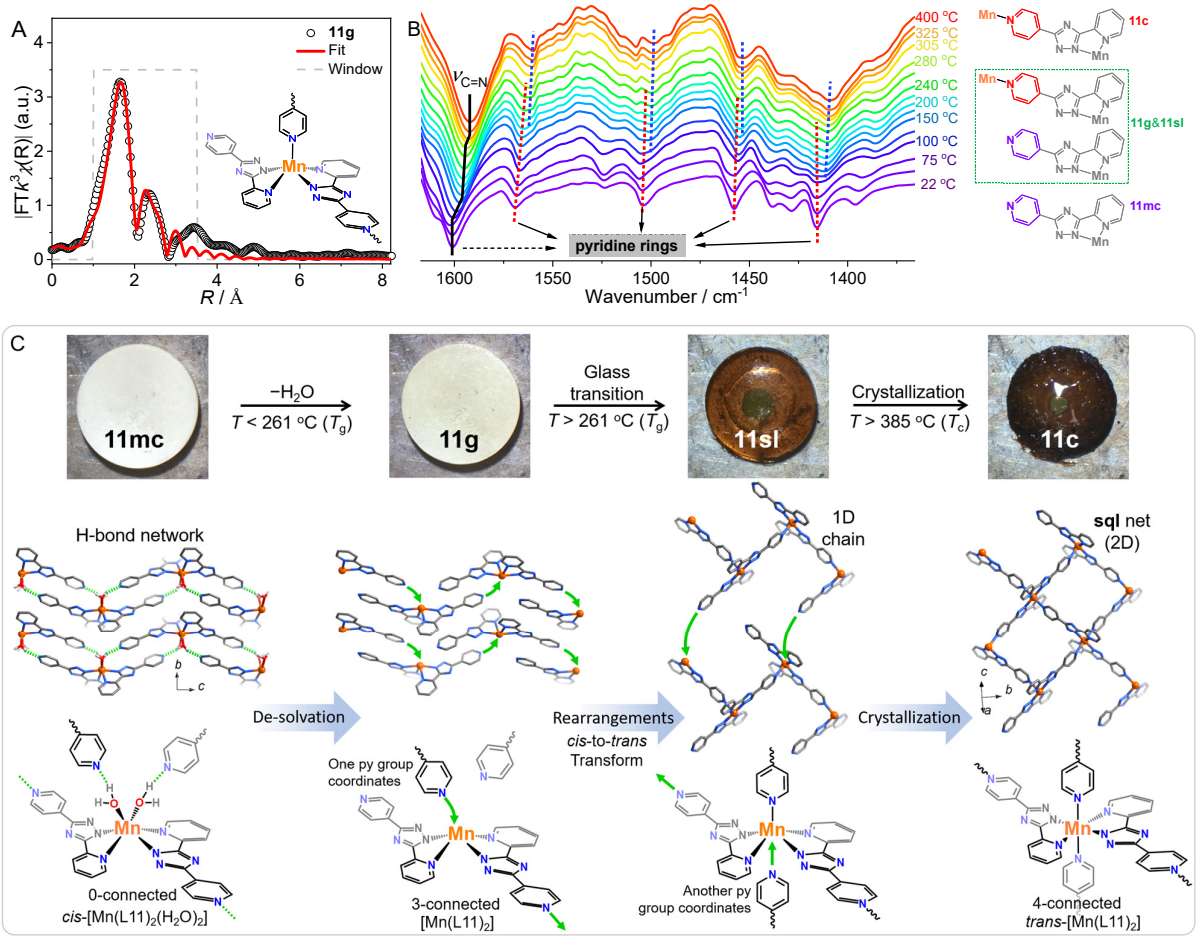

Fig. 4. Structural transformation upon 11mc during heating. (**A**) Mn *K*-edge EXAFS fitting curve of **1g**. Insert: proposed architecture of the coordination environment around Mn(II). (**B**) Variable temperature FT-IR spectra upon **1mc**. The peak shifts are highlighted by the dotted lines. (**C**) Top: Optical images of heat-induced transformation from white pellet (**11mc**), light yellow pellet (**11g**), brown transparent monolith (**11sl**) to dark monolith (**11c**). Proposed transformation upon **11mc** of packing structures (Middle) and coordination environments around Mn(II) (Bottom) during the de-solvation and crystallization processes.

Porosity analysis with the glass structures

De-solvation strategy successfully yielded MOF glasses of different dimensions, offering a valuable platform to explore the correlation between porosity and glass structures. Sorption isotherms of selective glasses were measured with different kinetic diameters of gases: CO_2 (3.3 Å), N_2 (3.6 Å) and C_2H_6 (4.1 Å). For the case of **1g** in Fig. 5A, the total uptakes at 1 bar of CO_2 (40.4 $cm^3\ g^{-1}$ at 195 K), N_2 (12.4 $cm^3\ g^{-1}$ at 77 K) and C_2H_6 (1.5 $cm^3\ g^{-1}$ at 195 K) follow the opposite trend in kinetic diameters of the gases, indicating the permanent accessible porosity in **1g**. The CO_2 sorption isotherm (Fig. 5B) at 195 K of **3g** exhibited a total uptake of 50.0 $cm^3\ g^{-1}$ at 1 bar with BET surface area of 162.8 $m^2\ g^{-1}$ and pore volume of 0.089 $cm^3\ g^{-1}$, higher than these of **1g**. For C_2H_6 as the biggest probe molecule, **3g** still showed an obvious uptake of 23.9 $cm^3\ g^{-1}$ at 1 bar and 195 K, while **1g** had a negligible uptake. The pore size enhancement from **3g** to **1g** should be due to the extended linker with the same underlying **rtl**-topology (*39*). However, **3g** showed almost no N_2 adsorption at 77 K, possibly owing to further shrinkage of the **rtl** network at such lower temperature (i.e. thermal expansion) (*40*). **10g** and **10c** showed multi-step gate-opening CO_2 sorption behaviors (Fig. 5C), indicating the dynamic slippage of their layered structures upon gas inclusion (*41*). In the cases of **11g** and **12g**, the similar profiles of CO_2 sorption isotherms with total uptakes of 62.8 and 72 $cm^3\ g^{-1}$ at 1 bar demonstrated their porous 1D chain networks (Figs. 5D and S51). The 2D structure of **11c** was also confirmed by its gate-opening gas sorption behavior. To our knowledge, these pore size fine-tuning and dynamic structural changes upon gas inclusions haven't been observed in reported MOF glasses (*42-44*).

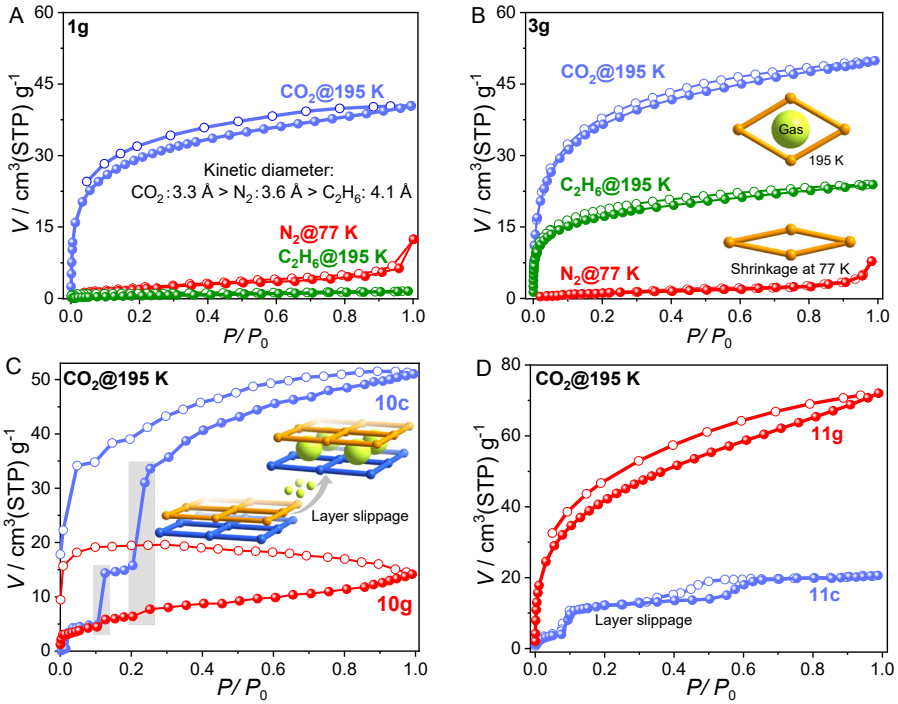

Fig. 5. Gas sorption properties. (**A**,**B**) Sorption of CO_2 at 195 K (blue), N_2 at 77 K (red) and C_2H_6 at 195 K (green) for **1g** (A) and **3g** (B). Insert of **B**: Schematic models for the flexible framework of **3g** upon temperature (**C**,**D**) Sorption of CO_2 at 195 K for **10g** (red) and **10c** (blue) (C) as well as **11g** (red) and **11c** (blue) (D). Insert of **C**: Schematic sliding

layered structures of **10g** upon gas molecules. Adsorption and desorption are shown by close and open symbols, respectively.

CONCLUSION

We have developed an approach for the general construction of glass states of metal-carboxylate frameworks, in which the hydrogen-bonded assemblies of discrete complexes guided the glass-networking behaviors during de-solvation. The de-solvation strategy allowed to acquire rational design concepts to fine-tune MOF glass structures including chemical composition, structure topology and functionality, and glass-forming ability-properties impossible to be customized via conventional vitrification. This systematic work opens up new avenues for the designing network structures of glassy states which has been one of the biggest challenges in amorphous sciences.

References

1. T. D. Bennett, S. Horike, *Nat. Rev. Mater.* **3**, 431-440 (2018).
2. N. Ma, S. Horike, *Chem. Rev.* **122**, 4163-4203 (2022).
3. M. Eddaoudi, J. Kim, N. Rosi, D. Vodak, J. Wachter, M. O'Keeffe, O. M. Yaghi, *Science* **295**, 469-472 (2002).
4. J.-P. Zhang, Y.-B. Zhang, J.-B. Lin, X.-M. Chen, *Chem. Rev.* **112**, 1001-1033 (2012).
5. H. Deng, C. J. Doonan, H. Furukawa, R. B. Ferreira, J. Towne, C. B. Knobler, B. Wang, O. M. Yaghi, *Science* **327**, 846-850 (2010).
6. D. Umeyama, S. Horike, M. Inukai, T. Itakura, S. Kitagawa, *J. Am. Chem. Soc.* **137**, 864-870 (2015).
7. T. D. Bennett, J.-C. Tan, Y. Yue, E. Baxter, C. Ducati, N. J. Terrill, H. H. M. Yeung, Z. Zhou, W. Chen, S. Henke, A. K. Cheetham, G. N. Greaves, *Nat. Commun.* **6**, 8079 (2015).
8. W. Chen, S. Horike, D. Umeyama, N. Ogiwara, T. Itakura, C. Tassel, Y. Goto, H. Kageyama, S. Kitagawa, *Angew. Chem., Int. Ed.* **55**, 5195-5200 (2016).
9. T. To, S. S. Sørensen, M. Stepniewska, A. Qiao, L. R. Jensen, M. Bauchy, Y. Yue, M. M. Smedskjaer, *Nat. Commun.* **11**, 2593 (2020).
10. J. Hou, P. Chen, A. Shukla, A. Krajnc, T. Wang, X. Li, R. Doasa, L. H. G. Tizei, B. Chan, D. N. Johnstone, R. Lin, T. U. Schülli, I. Martens, D. Appadoo, M. S. Ari, Z. Wang, T. Wei, S.-C. Lo, M. Lu, S. Li, E. B. Namdas, G. Mali, A. K. Cheetham, S. M. Collins, V. Chen, L. Wang, T. D. Bennett, *Science* **374**, 621-625 (2021).
11. R. S. K. Madsen, A. Qiao, J. Sen, I. Hung, K. Chen, Z. Gan, S. Sen, Y. Yue, *Science* **367**, 1473-1476 (2020).
12. B. K. Shaw, A. R. Hughes, M. Ducamp, S. Moss, A. Debnath, A. F. Sapnik, M. F. Thorne, L. N. McHugh, A. Pugliese, D. S. Keeble, P. Chater, J. M. Bermudez-Garcia, X. Moya, S. K. Saha, D. A. Keen, F.-X. Coudert, F. Blanc, T. D. Bennett, *Nat. Chem.* **13**, 778-785 (2021).
13. Z. Yin, Y. Zhao, S. Wan, J. Yang, Z. Shi, S.-X. Peng, M.-Z. Chen, T.-Y. Xie, T.-W. Zeng, O. Yamamuro, M. Nirei, H. Akiba, Y.-B. Zhang, H.-B. Yu, M.-H. Zeng, *J. Am. Chem. Soc.* **144**, 13021-13025 (2022).
14. Y. Zhao, S.-Y. Lee, N. Becknell, O. M. Yaghi, C. A. Angell, *J. Am. Chem. Soc.* **138**, 10818-10821 (2016).
15. S. J. Yang, C. R. Park, *Adv. Mater.* **24**, 4010-4013 (2012).
16. T. Panda, S. Horike, K. Hagi, N. Ogiwara, K. Kadota, T. Itakura, M. Tsujimoto, S. Kitagawa, *Angew. Chem., Int. Ed.* **56**, 2413-2417 (2017).
17. T. D. Bennett, T. K. Todorova, E. F. Baxter, D. G. Reid, C. Gervais, B. Bueken, B. Van de Voorde, D. De Vos, D. A. Keen, C. Mellot-Draznieks, *Phys. Chem. Chem. Phys.* **18**, 2192-2201 (2016).
18. D. Lässig, J. Lincke, R. Gerhardt, H. Krautscheid, *Inorg. Chem.* **51**, 6180-6189 (2012).

19. J. F. Willart, F. Danede, A. De Gusseme, M. Descamps, C. Neves, *J. Phys. Chem. B* **107**, 11158-11162 (2003).
20. H.-Q. Hao, M.-X. Peng, Z.-Y. Chen, *Acta Crystallogr. E* **63**, m2605-m2605 (2007).
21. K. I. Hadjiivanov, D. A. Panayotov, M. Y. Mihaylov, E. Z. Ivanova, K. K. Chakarova, S. M. Andonova, N. L. Drenchev, *Chem. Rev.* **121**, 1286-1424 (2021).
22. M. Cortijo, S. Herrero, R. Jiménez-Aparicio, J. Perles, J. L. Priego, M. J. Torralvo, J. Torroba, *Eur. J. Inorg. Chem.* **2013**, 2580-2590 (2013).
23. Q. Wei, M. Nieuwenhuyzen, F. Meunier, C. Hardacre, S. L. James, *Dalton trans.*, 1807-1811 (2004).
24. S. Horike, S. S. Nagarkar, T. Ogawa, S. Kitagawa, *Angew. Chem., Int. Ed.* **59**, 6652-6664 (2020).
25. S. K. Elsaidi, M. H. Mohamed, L. Wojtas, A. Chanthapally, T. Pham, B. Space, J. J. Vittal, M. J. Zaworotko, *J. Am. Chem. Soc.* **136**, 5072-5077 (2014).
26. T.-B. Lu, R. L. Luck, *Inorganica Chim. Acta* **351**, 345-355 (2003).
27. Z. Chen, G. Gallo, V. A. Sawant, T. Zhang, M. Zhu, L. Liang, A. Chanthapally, G. Bolla, H. S. Quah, X. Liu, K. P. Loh, R. E. Dinnebier, Q.-H. Xu, J. J. Vittal, *Angew. Chem., Int. Ed.* **59**, 833-838 (2020).
28. P. Pachfule, Y. Chen, J. Jiang, R. Banerjee, *Eur. J. Chem.* **18**, 688-694 (2012).
29. W.-J. Feng, G.-P. Zhou, X.-F. Zheng, Y.-G. Liu, Y. Xu, *Acta Crystallogr. E* **62**, m2033-m2035 (2006).
30. K.-H. Cui, S.-Y. Yao, H.-Q. Li, Y.-T. Li, H.-P. Zhao, C.-J. Jiang, Y.-Q. Tian, *CrystEngComm* **13**, 3432-3437 (2011).
31. J.-B. Lin, J.-P. Zhang, W.-X. Zhang, W. Xue, D.-X. Xue, X.-M. Chen, *Inorg. Chem.* **48**, 6652-6660 (2009).
32. J.-B. Lin, J.-P. Zhang, X.-M. Chen, *J. Am. Chem. Soc.* **132**, 6654-6656 (2010).
33. R. S. K. Madsen, S. Sarkar, B. B. Iversen, Y. Yue, *Chem. Commun.* **58**, 823-826 (2022).
34. J. Hou, M. L. Ríos Gómez, A. Krajnc, A. McCaul, S. Li, A. M. Bumstead, A. F. Sapnik, Z. Deng, R. Lin, P. A. Chater, D. S. Keeble, D. A. Keen, D. Appadoo, B. Chan, V. Chen, G. Mali, T. D. Bennett, *J. Am. Chem. Soc.* **142**, 3880-3890 (2020).
35. H.-Y. Kwon, D. C. Ashley, E. Jakubikova, *Dalton trans.* **50**, 14566-14575 (2021).
36. Q.-H. Zhou, M. Li, P. Yang, Y. Gu, *Macromol. Theory Simul.* **22**, 107-114 (2013).
37. T. Liu, D. Luo, D. Xu, H. Zeng, Z. Lin, *Dalton trans.* **42**, 368-371 (2013).
38. H. Zhou, M. Li, D. Li, J. Zhang, X. Chen, *Sci. China Chem.* **57**, 365-370 (2014).
39. H. Deng, S. Grunder, K. E. Cordova, C. Valente, H. Furukawa, M. Hmadeh, F. Gándara, A. C. Whalley, Z. Liu, S. Asahina, H. Kazumori, M. O'Keeffe, O. Terasaki, J. F. Stoddart, O. M. Yaghi, *Science* **336**, 1018-1023 (2012).
40. Y.-S. Wei, R.-B. Lin, P. Wang, P.-Q. Liao, C.-T. He, W. Xue, L. Hou, W.-X. Zhang, J.-P. Zhang, X.-M. Chen, *CrystEngComm* **16**, 6325-6330 (2014).
41. A. Kondo, H. Noguchi, L. Carlucci, D. M. Proserpio, G. Ciani, H. Kajiro, T. Ohba, H. Kanoh, K. Kaneko, *J. Am. Chem. Soc.* **129**, 12362-12363 (2007).
42. C. Zhou, L. Longley, A. Krajnc, G. J. Smales, A. Qiao, I. Erucar, C. M. Doherty, A. W. Thornton, A. J. Hill, C. W. Ashling, O. T. Qazvini, S. J. Lee, P. A. Chater, N. J. Terrill, A. J. Smith, Y. Yue, G. Mali, D. A. Keen, S. G. Telfer, T. D. Bennett, *Nat. Commun.* **9**, 5042 (2018).
43. L. Frentzel-Beyme, P. Kolodzeiski, J.-B. Weiß, A. Schneemann, S. Henke, *Nat. Commun.* **13**, 7750 (2022).
44. J. Li, J. Wang, Q. Li, M. Zhang, J. Li, C. Sun, S. Yuan, X. Feng, B. Wang, *Angew. Chem., Int. Ed.* **60**, 21304-21309 (2021).

Acknowledgements

The work was supported by the Japan Society of the Promotion of Science (JSPS) for a Grant-in-Aid for Scientific Research (B) (JP18H02032), Challenging Research (Exploratory) (JP19K22200), and Transformative Research Areas (A) "Supra-ceramics" (JP22H05147) from the Ministry of Education, Culture, Sports, Science and Technology, Japan. We acknowledge Aichi Synchrotron Radiation (AichiSR) BL11S2 (2020D6005) and SPring-8 BL14B2 beamlines for XAFS and AichiSR BL5S2 beamline for PDF (2021D3036).

Author contributions

S.H. and Y.-S.W. designed the project. Y.-S.W. synthesized metal complexes and prepared the glassy compounds. Y.-S.W. collected and analyzed powder & single crystal X-ray diffraction, thermalgravimetric analysis, differential scanning calorimetry, scanning electron microscopy, infrared spectroscopy, N_2 adsorption, synchrotron X-ray absorption and total scattering measurements. Z.F. helped the analysis of synchrotron data. C.L. helped the synthesis of metal complexes and powder X-ray diffraction measurements. S.H. and Y.-S.W. wrote the paper, and all the authors contributed to revising the paper.

Competing interests

The authors declare no competing interests.

Materials & Correspondence.

Correspondence and requests for materials should be addressed to S.H. or Y.-S.W.